Origin of Structural Degradation in Li-rich Layered Oxide Cathode

Tongchao Liu[1,7], Jiajie Liu[2,7], Luxi Li[3,7], Lei Yu[4], Jiecheng Diao[5], Tao Zhou[4], Shunning Li[2], Alvin Dai[1],

Wenguang Zhao[2], Yang Ren[3], Liguang Wang[3], Tianpin Wu[3], Rui Qi[2], Yinguo Xiao[2], Jiaxin Zheng[2],

Wonsuk Cha[3], Ross Harder[3], Ian Robinson[5,6], Jianguo Wen[4], Jun Lu[1*], Feng Pan[2*], Khalil Amine[1*]

[1]Chemical Sciences and Engineering Division, Argonne National Laboratory, Lemont, IL 60439, USA
[2]School of Advanced Materials, Peking University, Shenzhen Graduate School, Shenzhen 518055, China.
[3]X‑ray Science Division, Argonne National Laboratory, Lemont, IL 60439, USA
[4]Center for Nanoscale Materials, Argonne National Laboratory, Lemont, IL 60439, USA
[5]London Centre for Nanotechnology, University College London, London WC1E 6BT, U.K.
[6]Condensed Matter Physics and Materials Science Department, Brookhaven National Laboratory, Upton, New York 11793, United States
[7]These authors contributed equally to this work.

*Corresponding author: amine@anl.gov (K. A.); panfeng@pkusz.edu.cn (F. P.); junlu@anl.gov (J. L.);

Abstract:

Voltage fade prevents effective use of the excess capacity and represents the most crucial technical challenge faced by Li- and Mn-rich cathode materials (LMR) in modern batteries. Although oxygen release has been arguably considered as an initiator for the failure mechanism, its prerequisite driving force has yet to be fully understood. Herein, relying on the *in-situ* nanoscale sensitive coherent X-ray diffraction imaging (BCDI) technique, we are able to track the dynamic structure evolution of the LMR cathode. The results, surprisingly, reveal that continuous nanostrain accumulation arose from lattice displacement in nano-domain structures during cell operation is the original driving force for detrimental structure degradations together with oxygen loss that triggers the well-known rapid voltage decay in LMR. By further leveraging primary to multi-particle structure and electrode-level as well as atomic scale observations, we demonstrate that the heterogeneous nature of the LMR cathode inevitably causes pernicious phase displacement which cannot be eliminated by the previous trials. With these fundamental discoveries, we propose the structural design strategy to mitigate the lattice displacement and inhomogeneous electrochemical/structural evolutions, thereby achieving stable voltage and capacity profiles. These findings highlight the significance of lattice displacement in voltage

33 decay mechanism and will inspire a wave of efforts to unlock the potential of the broad-scale

34 commercialization of LMR cathode material.

35

36

37 **Introduction**

38   Li and Mn-rich cathode materials (LMR) that utilize both cation and anion redox are

39 among the very few options available to yield substantial increases in battery energy density.

40 However, voltage decay issues cause continuous energy loss and restrains the development of the

41 battery management system, the Achilles' Heel of this promising cathode material that impedes

42 its broad-scale commercialization[1-6]. While several prevailing theories have been established for

43 voltage fade, including transition metal (TM) migration, TM valence state reduction and

44 irreversible phase transitions, they are eventually attributed to thermodynamic instability of

45 lattice oxygen and to oxygen release.[7-11] Prior research efforts have also sought diverse solutions

46 to premeditatedly enhance lattice oxygen stability, however, the effectiveness of these strategies

47 is limited and it remains unresolved so far.[12-15] This predicament raises the suspicion of whether

48 thermodynamic instability is the governing prerequisite for voltage decay in the LMR cathode.

49   In conventional intercalation cathodes, Li ion (Li^+) movement in/out of its host

50 framework will drive dynamic structural evolution, which directly affects structure stability and

51 electrochemical profiles.[16-18] Unfortunately, uneven Li^+ (de)intercalation and heterogeneous

52 electrochemical reactions often occur in these cathodes, leading to nonequilibrium structural

53 dynamics at both the macroscopic and microscopic level.[19-21] The former is manifested as the

54 anisotropic volume variation and bulk mechanic strain that have been broadly viewed as the root

55 cause of mechanical degradation, such as secondary particle cracking[22,23]. The latter contributes

56 to nanoscale strain with less detectable lattice displacement[24], while their destructive effects on

57 topical structure stability remain unclear. This is particularly significant for LMR cathode

58 because its heterogeneous structure is composed of two structurally coherent nano-domains

59 ($LiTMO_2$ and Li_2MnO_3) that are electrochemically activated in separate voltage ranges with

60 different redox chemistries.[25-27] It is such heterogeneous structural dynamics of nano-domains

61 that determines the global generation of nanoscale strain that can substantially alter the structure

62 stability and aggravate oxygen release.

63 Despite its fundamental importance, lattice displacement and nanoscale strain are

64 probably the least understood structural properties in battery materials. Due to technical limits

65 faced in the past, characterization tools could not penetrate into nanoscale regimes, preventing

66 the observation of lattice displacement and the analysis of nanoscale strain[28]. This is even more

67 challenging that if we try to monitor the spatial strain evolution under operando conditions[20,29,30].

68 Clearly, building a mechanistic link between nanoscale structure dynamic and electrochemical

69 property requires systematic investigations spanning multiple length scales, which benefits to

70 unity the prior electrochemical degradation mechanism of LMR and guide effective approaches

71 to mitigating voltage fade.

72 Herein, we conduct a comprehensive investigation of nanoscale lattice evolution in LMR

73 cathode, revealing that lattice displacement and the resulting nanostrain are the root cause of

74 oxygen release prior to thermodynamic destabilization. By leveraging the combination of *in-situ*

75 nanoscale sensitive coherent X-ray diffraction, 3D rotation electron diffraction, and spinning

76 length X-ray diffraction techniques, we identify the heterogeneous nature of LMR as the

77 prerequisite for severe lattice displacement and the resulting nanostrain upon Li^+ (de)insertion.

78 Subsequently, continuous strain accumulation in nanoscale domains serves as the original

79 driving force triggering oxygen loss and detrimental structure degradation, which eventually

80 results in rapid voltage fade. Our results affirm that lattice displacement and nanostrain, which

81 represent commonly occurred but less detectable dynamic structure evolutions, play an

82 undeniable role in structure decomposition and voltage fade. Benefitting from these fundamental

83 discoveries, we propose to mitigate the voltage degradation of LMR with O2 phase based

84 cathode or a whole-voltage-range oxygen redox cathode that can effectively eliminate

85 inhomogeneous reactions and suppress strain generation. These findings provide more effective

86 structural strategies for preventing oxygen release and solving the long-standing voltage fade

87 issue.

88 **Initial structure and electrochemical properties**

89 The synthesis of $Li_{1.2}Ni_{0.13}Mn_{0.54}Co_{0.13}O_2$, a typical LMR cathode material is described in

90 the Method section. Synthesis of primary particle, rather than secondary particles, was

91 purposefully controlled for minimizing interference from morphological factors[31].

92 Supplementary Fig. 1 shows a single-particle morphology with sizes ranging from 300 to 600 nm,

93 which is an ideal size for the Bragg coherent diffraction imaging (BCDI) measurements. Data in

94   Supplementary Fig. 2 confirms that the composition of as-prepared sample was close to the
95   designed composition. The X-ray powder diffraction (XRD) measurement (Fig. 1a) shows
96   identical result as reported in the literature.[27] Characteristic super-reflections present in the 2θ
97   region of 1.4 to 2° correspond to Li/Mn ordering in the TM slabs (Li_2MnO_3-like phase). The
98   XRD pattern is further refined using the two-phase model, which consists of both rhombohedral
99    $R\bar{3}m$ and monoclinic C2/m phases that are present in LMR cathodes. More information can be
100   found in Supplementary Table 1.

101   Aberration-corrected scanning transmission electron microscope (AC-STEM) is applied
102   to directly visualize the spatial distribution of $LiTMO_2$ and Li_2MnO_3 domains. Fig.1c-Fig.1e
103   illustrate a typical layered structure with two types of bright spot arrangement. Those with
104   regular "bright-bright-dark" arrangements are identified as Li_2MnO_3 domains, which are
105   characterized by the well-known honeycomb Li-Mn ordering. The others with no distinguished
106   dark spots in the bright spot columns are identified as $LiTMO_2$ domains. It is clear that $LiTMO_2$
107   domains are three-dimensionally incorporated into the Li_2MnO_3 lattice without obvious
108   interphase boundaries, indicating that these two phases are randomly mixed and share the
109   coherent lattice structure.

110   The electrochemical profile of the LMR shows a high discharge capacity of 273 mAh g^{-1}
111   (Fig. 1b), which is very competitive against the current commercial cathode materials with high
112   Ni content.[32,33] Notably, two distinct electrochemical stages at different voltage ranges were
113   observed from the first charge profile as well as the corresponding *dQ/dV* curve (Supplementary
114   Fig. 3 and Fig. 4). Stage 1 is attributed to the activation of $LiTMO_2$ domains associated with the
115   oxidation of Ni and Co ions.[34] The extra charge capacity at a plateau voltage over 4.47 V is
116   defined as stage 2, in which the Li_2MnO_3 domains are activated with accompany of oxygen
117   release usually.[35,36] The electrochemical profile confirms the differential electrochemical
118   activities of these two structurally coherent domains. Galvanostatic Intermittent Titration
119   Technique (GITT, Supplementary Fig. 5) demonstrates that Li ion diffusion coefficient keeps
120   stable in stage 1 but dramatically decreases after the activation of Li_2MnO_3 domains (stage 2),
121   indicating that reaction kinetics involved in TM redox and oxygen redox are also significantly
122   different. Despite its attractive capacity, the LMR cathode is still facing significant challenges
123   for its commercialization in large scale. Fig. 1b illustrates that the so-called voltage fade and

124 capacity loss concurrently exhibit during prolonged cycling process, which causes a substantial
125 loss of energy density and the invalidation of the battery management system.

126 It is argued that the electrochemical degradation mechanism is closely related to the
127 synergy of structure decomposition and oxygen release[34]. However, the prerequisite driving
128 force of these detrimental reactions remain ambiguous. Previous studies also argued that oxygen-
129 related gas stems from the activation of thermodynamically unstable Li_2MnO_3 domains[34,37].
130 Paradoxically, recent density functional theory (DFT) calculation results demonstrate that
131 oxygen release is thermodynamically unfavorable in the initial delithiation of the pure
132 Li_2MnO_3.[38,39] To clarify the uncertainty shrouding oxygen release, we conducted differential
133 electrochemical mass spectrometry (DEMS) to measure the gas evolution of Li_2MnO_3 upon the
134 first charge under operando condition. Supplementary Fig. 6 shows that oxygen-related gas is
135 absent at the initial activation of Li_2MnO_3 around 4.5 V (less than 20% delithiation) and started
136 to be detected over 20% delithiation of Li_2MnO_3. This result provides direct evidence that the
137 activation of pure Li_2MnO_3 material is not the root cause of oxygen release. Consequently,
138 oxygen release mechanism of LMR cathode cannot be solely attributed to the activation of
139 Li_2MnO_3 domains and its thermodynamic instability. This also explained why the previous effort
140 to improve oxygen stability of LMR cathodes fails to solve the voltage fading issue. The
141 interaction between Li_2MnO_3 and $LiTMO_2$ is critical for oxygen release but it seems to be
142 overlooked previously.

143 As mentioned above, the $LiTMO_2$ and Li_2MnO_3 domains share a coherent lattice but
144 exhibit independent electrochemical activity at differentiated voltage ranges. Thus, there exists a
145 tremendous conflict between the coherent lattice and the inhomogeneous deintercalation
146 chemistry. Generally, in stage 1, extracting Li from $LiTMO_2$ domains will increase the
147 electrostatic repulsion of oxygen layers and result in lattice expansion as the structural response.
148 However, due to the electrochemically inactive nature of Li_2MnO_3 below 4.47 V, the lattice
149 expansion of $LiTMO_2$ will be partly confined by the surrounding Li_2MnO_3. This situation will
150 cause inhomogeneous lattice spacing and lattice displacement in the coherent structure. These
151 nonequilibrium structural responses can be collectively referred to as lattice strain at nanoscale.
152 In order to simplify it and distinguish it from the strain commonly used in conventional XRD, we
153 define nanoscale lattice strain as nanostrain. Differing from the macroscopic mechanic strain,
154 nanostrain imposed at the junction of two nano-domains can substantially alter the structure

155 stability. With continuous delithiation, nanostrain will gradually accumulate and globally exist in

156 the bulk structure, which may trigger structure decomposition such as oxygen release and

157 irreversible phase transition. Although it shows potential significance for structure stability, the

158 nanostrain, which manifests as extremely small lattice displacement (less than nm) was rarely

159 investigated in battery materials mainly due to the characterization limit. Conventional XRD is

160 capable of detecting strain but tends to underestimate local strain as it averages over a large area.

161 Therefore, the in-operando investigation of nanostrain is of particular interest for the mechanism

162 understanding of structure decomposition and oxygen release in LMR cathodes.

163

Strain evolution of the single LMR particle through BCDI

165 The Bragg coherent X-ray diffraction imaging (BCDI) is an invaluable method to study

166 the structural, morphological and lattice strain information in single crystal materials.[40]

167 Benefitting from the high penetration power of X-rays, BCDI has becomes an indispensable tool

168 to visualize nonequilibrium lattice evolution in electrode materials under operando

169 conditions.[31,40,41]. Hence, BCDI measurements are performed to monitor lattice displacement and

170 analyze strain evolution of the LMR primary particle during electrochemical reactions. The

171 experimental setup is illustrated in Method section. Focused coherent X-rays impinge onto an in-

172 situ coin-cell and the 3D diffraction patterns of the [003] reflection from an LMR primary

173 particle are recorded repeatedly as angle-rocking scans by an area detector throughout the initial

174 charge process[42]. These 3D diffraction patterns are analyzed using a combination of the Error

175 Reduction and the Hybrid Input/Output algorithms to reconstruct the 3D structure and the lattice

176 displacement along the momentum transfer direction, which is the particle c-axis here.

177 Henceforth in this work, we will refer to images if this lattice displacement as generic "strain"

178 although it is technically an integral of strain.[24]

179 In Fig. 2a, to demonstrate the spatial lattice evolution of the cathode material, the

180 reconstructed LMR primary particle is displayed as three-dimensional cross-section images, in

181 which the negative and positive lattice displacements (compressive and tensile nanostrains) are

182 expressed by blue and red, respectively. In the pristine stage (Fig. 2b), we observed the

183 concurrent appearance of both compressive and tensile nanostrain. We believe these initial

184 strains are due to local Li aggregation and vacancies caused by high temperature sintering

185 process. The initial strain gradually disappears with initial delithiation as rearrangement of Li

186 occupancies in Li layers (Fig. 2c). When entering the first voltage slope around 3.9V (Fig. 2d), a
187 tensile nanostrain begins to present itself on the particle surface. As discussed above, the initial
188 Li extraction predominately occurs in the $LiTMO_2$ domains and results in local lattice expansion.
189 The lattice expansion is partly confined by the inactive Li_2MnO_3, which results in tensile
190 nanostrain. The tensile nanostrain occurs preferentially near particle surface area which makes
191 sense since Li extraction starts there. With continuous Li extraction, the tensile nanostrain
192 gradually accumulates and extends into the interior of the particle (Fig. 2e-2h). At the end of
193 stage 1 (4.43V), where almost all $LiTMO_2$ domains are fully delithiated, the electrostatic
194 repulsion between oxygen layers reached the maximum, resulting in the global existence of
195 tensile strain in the entire particle (Fig. 3a). Therefore, undergoing such inhomogeneous Li
196 concentration and accumulated tensile nanostrain severely affects the structural stability of the
197 composite LMR, which may trigger the decomposition of Li_2MnO_3 domains.

198   Interestingly, the lattice displacement evolution reverses once entering stage 2. Fig. 3b
199 shows the tensile nanostrain started to decrease at 4.46 V, which is considered as the starting
200 voltage of the Li_2MnO_3 domains activation and the onset of O_2 release. To verify this, *in-situ*
201 DEMS is carried out to measure the gas generation during the first charge. Fig. 3e shows
202 oxygen-related gas is not evolved in stage 1. Once entering stage 2, the onsets of O_2 and CO_2
203 signals are simultaneously observed, which is exactly consistent with the above-mentioned
204 displacement weakening and strain changes. The overall tensile nanostrain gradually decreases
205 with oxygen release in stage 2, until the particles disappeared from the detection field at 4.51 V
206 (Fig. 3c-3d). As a consequence, the correlation between lattice displacement evolution and
207 oxygen release is naturally established. The inhomogeneous electrochemical kinetics of two
208 domains results in globally existed lattice displacement, nanostrain accumulation and
209 tremendous inhomogeneity of Li^+ concentration, which will accelerate the decomposition of
210 Li_2MnO_3 and trigger oxygen release. After oxygen release, the confined lattice expansion relaxes
211 and in turn leads to the decrease of lattice displacement. This argument is further supported by
212 the results of the DFT calculation. Fig. 3f and 3g indicates the energy barriers to remove lattice
213 oxygen will be significantly reduced when the increased tensile nanostrain is applied to the
214 Li_2MnO_3 domains.

215 **Origin and relaxation of tensile nanostrain in the LMR cathode**

216   To build the mechanistic link between lattice displacement and electrochemical reaction,

217   systematic structure characterization spanning multiple length scales were performed to

218   investigate structure evolution of LMR cathode during the first cycle (Fig. 4a). Firstly, the *in-situ*

219   coherent X-ray multi-crystal diffraction technique (CMCD) is applied to monitor the minuscule

220   phase evolutions of LMR cathode during operando operation[42]. With just tens of particles giving

221   diffraction signals, CMCD can record semi-statistical information on the structure transmissions

222   of LMR particles and the response of individual crystals that are typically not visible in

223   conventional XRD. This technique benefits from a unique vision between the macroscopic and

224   the microscopic and fills in the capability gap between conventional XRD and BCDI (Fig. 4a).

225   As can be seen in Fig. 4b, the Debye-Scherrer ring of the (003) peak is selected to track the

226   structure evolution and lattice changes, which is consistent with the reflection of BCDI. The

227   image captured at OCV shows a single ring composed of a series of bright diffraction spots (D_1)

228   that corresponds to the *c-axis* reflection of tens of primary particles. Since the single-phase

229   reaction of $LiTMO_2$ domains is below 4.47 V, the diffraction ring did not undergo obvious

230   changes. When the battery was charged to 4.472 V that corresponds to the initial voltage of

231   oxygen release, a bright diffraction spot appears at a smaller angle (D_2), which suggests that part

232   of a particle undergoes lattice expansion with oxygen release. This reaction should be attributed

233   to the activation of Li_2MnO_3 domains and lead to the relaxation of confined lattice expansion.

234   Further charging to 4.484 V leads to more diffraction spots moving towards smaller angle. At the

235   later stage of the O-redox plateau, these diffraction spots integrate to a clear powder ring (D_2) at

236   4.562 V. The powder ring of D_2 keeps intensifying along with the charging and its intensity

237   reaches the maximum at 4.8 V. Meanwhile, the original powder ring (D_1) weakens as the new

238   powder ring intensifies.

239   The CMCD results clearly reflects the inhomogeneous lattice expansion behavior of the

240   LMR cathode during the first charge. In stage 1 (below 4.472 V), due to the surrounding inactive

241   Li_2MnO_3 domains, the lattice expansion is partly confined and only presents one diffraction ring.

242   Such inhomogeneous structure evolution of two domains is the primary cause of the lattice

243   displacement observed in the BCDI images. As lattice displacement gradually increases, the

244   Li_2MnO_3 domains is struggling with the imposed tensile nanostrain and Li^+ concentration

245   imbalance, which subsequently triggers the decomposition of Li_2MnO_3. The confined lattice

expansion is released naturally with the activation of Li_2MnO_3 domains, leading to the relaxation of tensile nanostrain. With more Li_2MnO_3 domains decomposing in the following charging process, a growing number of lattices are liberated and expand along the c axis, which is reflected in the brighter spots appearing in the second diffraction ring (D_2). In the end of charge (4.8 V), the intensity of D_2 reaches the maximum, suggesting most of Li_2MnO_3 domains are "activated".

During the discharge process, the reflection in the CMCD images converts back to the original single diffraction ring (D_1) via the converse sequence of structure transitions. Interestingly, in addition to D_2 and D_1 rings, another weak diffraction ring (D_3) is visualized in even smaller diffraction angle at the very beginning of discharge. This diffraction ring can be indexed to the (101) crystal plane of $Li_2Mn_2O_4$, which is considered to be the phase formed by the overlithiation of spinel $Li_xMn_2O_4$. This observation implies that transition metal migration to Li layers occurs with oxygen release and $Li_xMn_2O_4$ spinel-like phase forms in the first charge. The diffraction ring of D_3 only appeared in the first 10 minutes of discharge (vs. a total of 10 hours discharge time), which suggests the $Li_2Mn_2O_4$ is a kinetic-dependent intermediate phase. In this sense, we infer that those $Li_xMn_2O_4$-like spinel domains are most likely concentrated on the particle surface that are momentarily over-lithiated to form $Li_2Mn_2O_4$ due to the high Li ion concentration and poor Li diffusion of the surface at the beginning of discharge. As lithium ions gradually migrate to the bulk, the over-lithiated $Li_2Mn_2O_4$ gradually change to $LiMn_2O_4$, whose diffraction ring is very close to D_1 and D_2. Thus, the diffraction ring of D_3 accordingly disappears with surface Li^+ concentration equilibrium.

Concurrently, high-energy ex-situ XRD was further conducted to macroscopically investigate the correlation between structural evolution and electrochemical properties. As seen in Fig. 4c, (003) peak shift towards the lower diffraction angle before 4.45 V, which is associated with the lattice expansion induced by $LiTMO_2$ domains. When charged to 4.45 V, corresponding to the beginning voltage of oxygen release, obvious (003) peak broadening started to be visualized, indicating that the confined lattice expansion is released with the decomposition of Li_2MnO_3 domains. These statistical observations of structure evolution are consistent with the appearance of the second diffraction ring (D_2) in the CMCD images. At the same time, the disappearance of the superlattice peak over 4.5 V (Supplementary Fig. 7) suggests that TM

9

migration must occur with oxygen release and the TM ordering is broken. This argument is further supported by the *ex-situ* extended X-ray absorption fine structure (EXAFS) and the fitting results. Supplementary Fig. 8 and Table 2 show that the coordination number of Mn-O evidently decreases but that of Mn-TM increases accordingly. This again confirms that lattice displacement and nanostrain accumulation will trigger TM migration and oxygen release. More importantly, the broadening and weakening of a series of peaks are found to be mainly related to *c* axis, such as (003), (104), (107) and (108) peaks (Fig. 4c and Supplementary Fig. 7). The oriented peak broadening is due to more inhomogeneous lattice changes occurring along the *c*-axis during charge/discharge, which further confirmed that nanostrain evolution stems from the heterogeneous nature of LMR cathode.

Atomic observation of lattice displacement and chemical state evolution.

To visually investigate the lattice displacement and nanostructure evolution, transmission electron microscope (TEM), 3D rotation electron diffraction (3D-rED) and electron energy loss spectroscopy (EELS) are performed on the delithiated samples. As mentioned above, the inhomogeneous electrochemical activities and structure evolution of two domains result in lattice displacement and nanostrain. In the microscopic vision, lattice displacement can be captured by a high resolution TEM. Fig. 5a-5c and Supplementary Fig. 9 show that although layered structure is maintained at 4.47 V, obvious lattice displacement presents on the surface and the bulk as well. For example, the lattices in the marked areas are deformed significantly. Likewise, more obvious displacement occurs on the surface with constant lattice twist (Fig. 5c), which is consistent with the observation of BCDI.

When entering stage 2, a continuous delithiation is accompanied by oxygen release together with the activation of Li_2MnO_3 domains. The same observation is conducted to track the lattice changes after Li_2MnO_3 activation. Supplementary Fig. 10 demonstrates that beside lattice displacement, a phase transition from layered structure to spinel phase occurs in this stage (4.5V). The lattice evolution in a larger scale were further investigated by 3D-rED in reciprocal space that recently was applied to study battery materials (Fig. 5d and Supplementary Figs. 11-12)[43]. The experimental details can be found in the Method section. Fig. 5e-5f illustrates that obviously twisted reflections along the *c* axis is observed in the reconstructed discrete reciprocal lattice.

These twisted diffraction points could be attributed to the lattice displacement observed in the high resolution TEM. Structure identification are analyzed using the selected area electron diffraction (SAED). As shown in Fig. 5g and Supplementary Fig. 13, in addition to typical layered structure and weak Li_2MnO_3 reflection, we also observed the reflection that corresponds to spinel lattice. This further confirmed the severe lattice displacement will trigger transition metal migration and structure transition from layered phase to spinel phase. These observations are in good agreement with the structure evolution captured by CMCD.

TEM combining EELS is used to precisely probe the structural and chemical variation of the fully delithiated sample (4.8 V). As shown in Fig. 5h and Supplementary Fig. 14, TEM again confirms the occurrence of structure transition, especially on the surface of the particle. A clear reconstruction surface layer with spinel and rock-salt phase is the direct evidence of transition metal migration and irreversible phase transition after oxygen release. EELS line profiles of O-K edge and Mn-$L_{2,3}$ were stacked in Fig. 5i, 5j and Supplementary Fig. 15 along the bulk to the surface. The intensity of O-K edge prepeaks substantially reduces from the interior to the exterior and almost disappears near the surface. Likewise, the O-K line-scan parallel to the surface (Supplementary Fig. 16) further confirms that the oxygen release uniformly occurs in the entire particle surface as the O prepeak disappears. It is worth noting that the oxygen release predominately occurs near the surface, where the lattice displacement evolves most drastically during the first charge, verifying that lattice displacement and resulting strain accumulation is the root cause of oxygen release. Concurrently, Mn L edge shows left shift near the surface (Fig. 5j). 2D EELS mapping further reverts the chemical state change of Mn in the whole particle (Fig. 5k). It is evident that the surface reconstruction layer shows a relatively lower Mn valance than the bulk, which suggests that Mn oxidation state decreases occur with its migration and oxygen release near the surface. Based on the above observation, the oxygen release and transition metal migration occur preferentially in regions where the structure suffers from severe lattice displacement, suggesting that these destructive reactions are primarily rooted in lattice displacement.

A prospect for the future development of Li- and Mn-rich cathode materials

The prevailing theories established for the voltage fade are thermodynamic instability of structure with the tendency to oxygen release and progressive structural rearrangement involving

335 TM migration and irreversible phase transitions.[15, 44] However, there are significant confusions

336 over these aspects. First, the presumption that thermodynamic instability triggers oxygen release

337 is not supported by DFT calculation results and the origin of oxygen release remains unclear.[38, 39]

338 In addition, TM migration and irreversible phase transition is limited near surface area from

339 TEM observation and invisible in the macroscopic characterizations.[45, 46, 47] This calls into

340 question whether such local structural degradation can undermine the overall electrochemical

341 behaviors. In this work, we dig into the dynamic nanostructure evolution and the local interaction

342 of the domain structures, which are not accessible previously. Combining the multiscale

343 characterizations and DFT calculation, we revealed that lattice displacement induced by

344 nonequilibrium structural dynamics is the root driving force of voltage fade. More importantly,

345 lattice displacement and nanostrain evolution provides a plausible explanation for the origin of

346 oxygen release and TM migration, unifying previously proposed theories for voltage fade.

347   A strain-induced structure degradation mechanism is detailed in the schematic image (Fig.

348 6). In general, the different electrochemically reactivities but coherent lattice structure of two

349 domains constitutes a prerequisite for lattice displacement. The activation of $LiTMO_2$ increases

350 local electrostatic repulsion with a tendency of lattice expansion. Due to the electrochemical

351 isolation of the Li_2MnO_3 domains, their lattice expansion is partly confined, resulting in severe

352 nanostrain with lattice displacement. Nanostrain initiates from the particle surface, gradually

353 extends into the bulk of particle with continuous delithiation and reaches the maximum when the

354 $LiTMO_2$ domains are almost fully delithiated. The extreme nanostrain imposed on the particles

355 substantially decreases the structural stability, triggering the decomposition of Li_2MnO_3 and

356 oxygen release. As the Li_2MnO_3 domains are activated, the imposed lattice expansion is

357 naturally released and tensile nanostrain relaxes synchronously. Likewise, oxygen release

358 significantly lowers the energy barrier of transition metal migration, resulting in irreversible

359 phase transition. Such strain evolution would adversely accumulate on long-term cycling, and

360 eventually lead to structural degradation and fast electrochemical decay.

361   The above mechanism demonstrates that the lattice displacement of the LMR cathode

362 originate from the heterogeneous composite structures and differential electrochemical activities.

363 Thus, post-treatments such as surface engineering methods show little effectiveness towards

364 voltage decay. Resolving this issue must fundamentally consider composition design or local

365　structure regulation. Practical approaches to tackle lattice displacement are to solve the

366　heterogenous structures of two composition in the LMR cathodes and their differential

367　electrochemical activities. Following this concept, we designed a O2 phase based

368　$Li_xNi_{0.13}Mn_{0.54}Co_{0.13}O_2$ cathode material that is characterized by eliminating composite domain

369　structure with homogeneous atomic arrangement (Supplementary Fig. 17). As a result, the

370　differential electrochemical activities are effectively suppressed, which is evidenced by a smooth

371　charging behavior with no apparently differentiated voltage plateaus (Supplementary Fig. 18).

372　Benefitting from the well-integrated electrochemical activities, the O2 phase based cathode

373　fundamentally eliminates the prerequisite for lattice displacement/strain generation, thereby

374　inhibiting oxygen release and achieving an enhanced electrochemical performance with stable

375　voltage profiles. This result in turn proves that the elimination of lattice displacement is essential

376　to solve the long-standing voltage fade issue. Other realistic strategies based on electrochemical

377　reactivities could also be promising. It will be more ideal if two types of redox reactions can be

378　completely blended, achieving a whole-voltage-range cationic/anionic hybrid redox cathode

379　material. This could not only eliminate the electrochemically inhomogeneous reactivity of two

380　domains, but also access to higher energy density, which potentially carries forward the practical

381　application of anionic redox or cationic/anionic hybrid cathode materials.

382

Conclusions

384　　　　With an innovative combination of 3D BCDI and 3D rED techniques, we thoroughly

385　investigated spatial and temporal nanostrain evolution of the LMR cathode during in-operando

386　conditions. A convincing mechanism that lattice displacement and strain accumulation trigger

387　oxygen loss and detrimental structure degradations is naturally established by leveraging gas

388　investigation and DFT calculation. The multiscale structure characterizations from CMCD and

389　macroscopic XRD further indicate that the inhomogeneous structure evolution in the coherent

390　lattice dominates the formation of lattice displacement and nanostrain accumulation. To

391　fundamentally resolve this issue, we propose that eliminating the electrochemically

392　inhomogeneous reactivity of two domains is crucial for suppressing lattice displacement and

393　subsequent electrochemical degradation. Structure design based on O2 phase and whole-voltage-

394　range oxygen redox cathode are considered as realistic strategies for resolving voltage fade.

395   These findings highlight the importance of the lattice displacement and strain accumulation in
396   the voltage decay mechanism and will serve as the guideline for seeking new solutions to
397   eliminate this issue.

398

399

Experiments:

Materials synthesis: The primary particle cathode materials of $Li_{1.2}Ni_{0.13}Mn_{0.54}Co_{0.13}O_2$ was synthesized using a sol-gel method. In a typical synthesis, $LiCH_3COO \cdot 2H_2O$ (Aladdin, 99%), $Ni(CH_3COO)_2 \cdot 4H_2O$ (Aladdin, 99%), $Co(CH_3COO)_2 \cdot 4H_2O$ (Aladdin, 99.5%), $Mn(CH_3COO)_2 \cdot 4H_2O$ (Aladdin, 99%) and Polyvinylpyrrolidone (Aladdin, K30) were mixed in a molar ratio of 9:1:1:4:30 and then dissolved in 100 mL of deionized water. The resulting solution was dried at 90 ^{o}C overnight under continuous stirring and then calcinated at 500 ^{o}C for 3 hours. The obtained powder was thoroughly ground and mixed in a mortar and then calcinated at 900 ^{o}C for 12 hours to obtain the final product.

Electrochemistry tests: For electrochemical testing, active materials were mixed with carbon black and PVDF at 80:10:10 wt % ratios and ground in a mortar. 2032 type coin cells were used to prepare lithium half cells. Celgard 2325 separators and 1.2 M $LiPF_6$ in EC / EMC (3:7) electrolyte (GEN II) were used. The half cells were then cycled between 2.0 and 4.8 V vs Li^+/Li, using small amounts of powder ($\sim$5.6 mg) as positive electrodes.

Bragg coherent X-ray diffraction imaging and coherent multiple crystal diffraction:

Bragg coherent diffraction data were collected at the 34-ID-C beamline of the Advanced Photon Source (APS). For the coherent diffraction analysis shown in this manuscript, we used 11.2 keV monochromatic beams in the in-situ BCDI experiment. The coherent X-ray beam was focused using a pair of Kirkpatrick−Baez (KB) mirrors to $\sim$1 × 1 μm^2 illuminating the LMR nanocrystals. The measurement was done on a 10 μm thick LMR electrode in transmission geometry. We used the same in situ coin-cell setup, which was implemented in the previous experiments with a window opening of 1 mm.[31] The coin cell was mounted on a coin cell holder vertically with the LMR electrode located downstream to minimize the absorption of the diffracted X-rays. The particle morphology of the LMR particles was examined with SEM, indicating 300−600 nm sized LMR particles (Supplementary Fig. 1). From the fringe spacing in the diffraction patterns, we estimated that the measured LMR nanoparticle size is approximately 600 nm.

Coherent X-ray multi-crystal diffraction (CMCD) patterns were acquired using a Timepix photon-counting detector mounted D = 1950 mm away from the sample. We obtained full rocking curves around the (003) Bragg reflection and collected 2D CMCD patterns using a 2D detector at two-theta angles of 18.6° ($\Delta\theta = \pm 0.15°$), respectively. Although the full sensor of the detector has 512×512 pixels with 55×55 m pixel size, the coherent diffraction patterns were collected utilizing just the first quadrant sensor, which has fewer bad pixels. Automatic background subtraction is implemented within the detector.[31] We collected 22 sets of CMCD patterns and each set includes 302 CMCD patterns by rocking the sample in 0.0025° steps around the Bragg peak while we were cycling the coin cell at the C/10 current rate (the C/10 rate is the current value discharge a battery in 20 h). Between consecutive scans, we optimized the sample position on a piezo scanning stage, to maintain the Bragg condition and avoid sample misalignment. The coin cell was cycled using an 8-channel MACCOR battery cycler while the series of measurements progressed.

Synchrotron X-ray diffraction, X-ray absorption spectroscopy measurement: Powder diffraction data of the cathode materials was collected using high-energy X-ray diffraction (HEXRD) located at sector 11-ID-C of the Advanced Photon Source at Argonne National Laboratory. A high-energy X-ray with a beam size of 0.2 mm×0.2 mm and wavelength of 0.1173 Å was used to obtain two-dimensional (2D) diffraction patterns in the transmission geometry. X-ray patterns were recorded with a Perkin-Elmer large-area detector placed at 1800 mm from the samples. Rietveld refinement of the collected HEXRD patterns was carried out using GSAS package. *Ex-situ* HEXRD measurements were performed at the same beamline. The electrodes were dissembled from the coin-cells charged or discharged to different potentials. With high penetration and low absorption, synchrotron HEXRD precisely reflects bulk sample structure properties, which is beneficial when observing tiny phase changes that usually are invisible from lab scale XRD due to poor background noise. To avoid peak interference from Al current collector, a freestanding LMR electrode was prepared from a mixture of LMR powder, carbon black and PTFE at 80:10:10 wt % ratios.

X-ray absorption near edge structure (XANES) and extended X-ray absorption fine structure (EXAFS) for Mn K-edge were performed at the APS on the bending-magnet beamline 9-BM-B. X-ray photon energy was monochromatized by an Si (111) double-crystal monochromator.

458 Higher-order harmonic contaminations were eliminated by detuning the monochromator to
459 reduce the incident X-ray intensity by approximately 30%. All spectra were collected at room
460 temperature in the transmission mode.

461 **Gas evolution analysis:** Differential electrochemical mass spectrometry (DEMS) was applied to
462 detect and identify gas evolution of different cathode materials during first charge/discharge. A
463 homemade cell with glass fiber separators and 1.2 M $LiPF_6$ in EC / EMC (3:7) electrolyte (GEN
464 II) was used for *in-situ* measurements. The cells were then cycled at a current rate of C/10
465 between 2.0 and 4.8 V vs Li^+/Li, using small amounts of powders (~8 mg) as positive electrodes.

466 **Transmission electron microscopy measurement:** TEM and HRTEM were conducted using
467 the Argonne Chromatic Aberration-corrected TEM (ACAT) (a FEI Titan 80-300 ST with an
468 image aberration corrector to compensate for both spherical and chromatic aberrations) at an
469 accelerating voltage of 200 kV. The 3D-rotation electron diffraction (3D-rED) datasets were
470 acquired by stepwise tilting sample with a collection angle of -40° to 40°. The tilt step is 2°. The
471 reciprocal lattice pattern was then reconstructed and analyzed by a handwritten script.

472

Data availability

474 The data that support the findings of this study are available from the corresponding authors
475 upon reasonable request.

476

493

Additional information

495 Supplementary information is available in the online version of the paper. Reprints and
496 permissions information is available online at www.nature.com/reprints. Correspondence and
497 requests for materials should be addressed to J.L., F.P. and K.A.

498

Author contributions

500 T.L., J.Lu and K.A. conceived the idea and designed the experiments. T.L. and J.Liu
501 synthesized all the materials and conducted electrochemical measurements. Y.L., T.Z., Y.X.,
502 W.Z. and J.W. carried out the TEM, EELS, and 3D-rED results. T.L., A.D., T.W., L.W. and Y. R.
503 performed *ex-situ* synchrotron HEXRD and XAS. T.L., L.L, J.D., W.C., R.H. and I.R. performed
504 *in-situ* BCDI, CMCD and data analysis. S.L., J.Z and F.P. conducted DFT calculation. T.L., J.Lu,
505 and K.A. wrote the manuscript and all authors edited the manuscript.

506

Competing financial interests

508 The authors declare no competing financial interests.

509

References

1   Li, M. *et al.* Cationic and anionic redox in lithium-ion based batteries. *Chem. Soc. Rev.* **49**, 1688-1705 (2020).

2   Hu, E. *et al.* Evolution of redox couples in Li-and Mn-rich cathode materials and mitigation of voltage fade by reducing oxygen release. *Nat. Energy* **3**, 690-698 (2018).

3   Assat, G. & Tarascon, J.-M. Fundamental understanding and practical challenges of anionic redox activity in Li-ion batteries. *Nat. Energy* **3**, 373-386, (2018).

4   Sathiya, M. *et al.* Reversible anionic redox chemistry in high-capacity layered-oxide electrodes. *Nat. Mater.* **12**, 827-835 (2013).

5   Zheng, J. *et al.* Li-and Mn-Rich Cathode Materials: Challenges to Commercialization. *Adv. Energy Mater.* **7**, 1601284 (2017).

6   Choi, J. W. & Aurbach, D. Promise and reality of post-lithium-ion batteries with high energy densities. *Nat. Rev. Mater.* **1**, 1-16 (2016).

7   Sathiya, M. *et al.* Origin of voltage decay in high-capacity layered oxide electrodes. *Nat. Mater.* **14**, 230-238 (2015).

8   Pearce, P. E. *et al.* Evidence for anionic redox activity in a tridimensional-ordered Li-rich positive electrode beta-Li_2IrO_3. *Nat. Mater.* **16**, 580-586 (2017).

9   Hong, J. *et al.* Metal-oxygen decoordination stabilizes anion redox in Li-rich oxides. *Nat. Mater.* **18**, 256-265 (2019).

10   Hu, S. *et al.* Insight of a Phase Compatible Surface Coating for Long-Durable Li-Rich Layered Oxide Cathode. *Adv. Energy Mater.* **9**, 1901795 (2019).

11   Shang, H. *et al.* Suppressing voltage decay of a lithium-rich cathode material by surface enrichment with atomic ruthenium. *ACS Appl. Mater. Interfaces* **10**, 21349-21355 (2018).

12   Singer, A. *et al.* Nucleation of dislocations and their dynamics in layered oxide cathode materials during battery charging. *Nat. Energy* **3**, 641-647, (2018).

13   Yan, P. *et al.* Injection of oxygen vacancies in the bulk lattice of layered cathodes. *Nat. Nanotechnol.* **14**, 602-608, (2019).

14   Assat, G. *et al.* Fundamental interplay between anionic/cationic redox governing the kinetics and thermodynamics of lithium-rich cathodes. *Nat. Commun.* **8**, 1-12 (2017).

15   Luo, K. *et al.* Charge-compensation in 3d-transition-metal-oxide intercalation cathodes through the generation of localized electron holes on oxygen. *Nat. Chem.* **8**, 684-691 (2016).

16   Liu, T. *et al.* Understanding Co roles towards developing Co-free Ni-rich cathodes for rechargeable batteries. *Nat. Energy* **6**, 277-286 (2021).

17   Liu, T. *et al.* Correlation between manganese dissolution and dynamic phase stability in spinel-based lithium-ion battery. *Nat. Commun.* **10**, 1-11 (2019).

18   Xu, C. *et al.* Bulk fatigue induced by surface reconstruction in layered Ni-rich cathodes for Li-ion batteries. *Nat. Mater.* **20**, 84-92 (2021).

19   Singer, A. *et al.* Nonequilibrium structural dynamics of nanoparticles in $LiNi_{1/2}Mn_{3/2}O_4$ cathode under operando conditions. *Nano Lett.* **14**, 5295-5300 (2014).

20   Ulvestad, A. *et al.* Topological defect dynamics in operando battery nanoparticles. *Science* **348**, 1344-1347 (2015).

21   Zhang, F. *et al.* Surface regulation enables high stability of single-crystal lithium-ion cathodes at high voltage. *Nat. Commun.* **11**, 1-11 (2020).

553   22   Bi, Y. *et al.* Reversible planar gliding and microcracking in a single-crystalline Ni-rich cathode.
554   *Science* **370**, 1313-1317 (2020).
555   23   Qian, G. *et al.* Understanding the Mesoscale Degradation in Nickel-Rich Cathode Materials
556   through Machine-Learning-Revealed Strain–Redox Decoupling. *ACS Energy Lett.* **6**, 687-693
557   (2021).
558   24   Robinson, I., & Harder, R. Coherent X-ray diffraction imaging of strain at the nanoscale. *Nat.*
559   *Mater.* **8**, 291-298 (2009).
560   25   Yoon, W.-S. *et al.* Local Structure and Cation Ordering in O3 Lithium Nickel Manganese Oxides
561   with Stoichiometry $Li[Ni_xMn_{(2-x)/3}Li_{(1-2x)/3}]O_2$: NMR Studies and First Principles Calculations.
562   *Electrochem. Solid State* **7**, A167–A171 (2004).
563   26   Yu, H. *et al.* Direct atomic-resolution observation of two phases in the $Li_{1.2}Mn_{0.567}Ni_{0.166}Co_{0.067}O_2$

564   cathode material for lithium-ion batteries. *Angew. Chem. Int. Ed.* **52**, 5969-5973 (2013).
565   27   Yu, X. *et al.* Understanding the rate capability of high-energy-density Li-rich layered
566          $Li_{1.2}Ni_{0.15}Co_{0.1}Mn_{0.55}O_2$ cathode materials. *Adv. Energy Mater.* **4**, 1300950 (2014).
567   28   Lin, F. *et al.* Synchrotron X-ray analytical techniques for studying materials electrochemistry in
568   rechargeable batteries. *Chem. Rev.* **117**, 13123-13186 (2017).
569   29   Ulvestad, A. *et al.* Single particle nanomechanics in operando batteries via lensless strain
570   mapping. *Nano Lett.* **14**, 5123-5127 (2014).
571   30   Jha, S. K., Charalambous, H., Okasinski, J. S., & Tsakalakos, T. Using in operando diffraction to
572   relate lattice strain with degradation mechanism in a NMC battery. *J. Mater. Sci.* **54**, 2358-2370
573   (2019).
574   31   Li, L., Xie, Y., Maxey, E. & Harder, R. Methods for operando coherent X-ray diffraction of battery
575   materials at the Advanced Photon Source. *J. Synchrotron Radiat.* **26**, 220-229 (2019).
576   32   Qiu, B. *et al.* Metastability and reversibility of anionic redox-based cathode for high-energy
577   rechargeable batteries. *Cell Rep. Phys. Sci.* **1**, 100028 (2020).
578   33   Li, W., Erickson, E. M., & Manthiram, A. High-nickel layered oxide cathodes for lithium-based
579   automotive batteries. *Nat. Energy* **5**, 26-34 (2021).
580   34   Zhao, S., Yan, K., Zhang, J., Sun, B., & Wang, G. Reaction Mechanisms of Layered Lithium-Rich
581   Cathode Materials for High-Energy Lithium-Ion Batteries. *Angew. Chem. Int. Ed.* **60**, 2208–2220
582   (2021).
583   35   Strehle, B. *et al.* The role of oxygen release from Li-and Mn-rich layered oxides during the first
584   cycles investigated by on-line electrochemical mass spectrometry. *J. Electrochem. Soc.* **164**,
585   A400-A406 (2017).
586   36   Nakayama, K., Ishikawa, R., Kobayashi, S., Shibata, N. & Ikuhara, Y. Dislocation and oxygen-
587   release driven delithiation in Li_2MnO_3. *Nat. Commun.* **11**, 1-7 (2020).
588   37   Rana, J. *et al.* Structural changes in Li_2MnO_3 cathode material for Li-Ion batteries. *Adv. Energy*
589   *Mater.* **4**, 1300998 (2014).
590   38   Xiao, R., Li, H. & Chen, L. Density functional investigation on Li_2MnO_3. *Chemistry of Materials* **24**,
591   4242-4251 (2012).
592   39   Chen, H. & Islam, M. S. Lithium extraction mechanism in Li-rich Li_2MnO_3 involving oxygen hole
593   formation and dimerization. *Chem. Mater.* **28**, 6656-6663 (2016).
594   40   Robinson, I., Vartanyants, I., Williams, G., Pfeifer, M., & Pitney, J. Reconstruction of the shapes
595   of gold nanocrystals using coherent x-ray diffraction. *Phys. Rev. Lett.*, **87**, 195505 (2001).
596   41   Robinson, I., & Harder, R. Coherent X-ray diffraction imaging of strain at the nanoscale. *Nat.*
597   *Mater.*, **8**, 291-298 (2009).

598   42   Ulvestad, A. *et al.* Single particle nanomechanics in operando batteries via lensless strain
599   mapping. *Nano Lett.* **14**, 5123-5127 (2014).
600   43   Li, J. *et al.* Structural origin of the high-voltage instability of lithium cobalt oxide. *Nat.*
601   *Nanotechnol.* **16**, 599-605 (2021).
602   44   Eum, D., *et al*. Voltage decay and redox asymmetry mitigation by reversible cation migration in
603   lithium-rich layered oxide electrodes. *Nat. Mater.* **19**, 419-427 (2020).
604   45   Liu, H., *et al.* Unraveling the rapid performance decay of layered high-energy cathodes: from
605   nanoscale degradation to drastic bulk evolution. *ACS Nano* **12**, 2708-2718 (2018).
606   46   Boulineau, A., Simonin, L., Colin, J. F., Bourbon, C. & Patoux, S. First evidence of manganese-
607   nickel segregation and densification upon cycling in Li-rich layered oxides for lithium batteries.
608   *Nano Lett.* **13**, 3857–3863 (2013).
609   47   Teufl, T., Strehle, B., Müller, P., Gasteiger, H. A. & Mendez, M. A. Oxygen Release and Surface
610   Degradation of Li- and Mn-Rich Layered Oxides in Variation of the Li_2MnO_3 Content. *J.*
611   *Electrochem. Soc.* **165**, A2718–A2731 (2018).
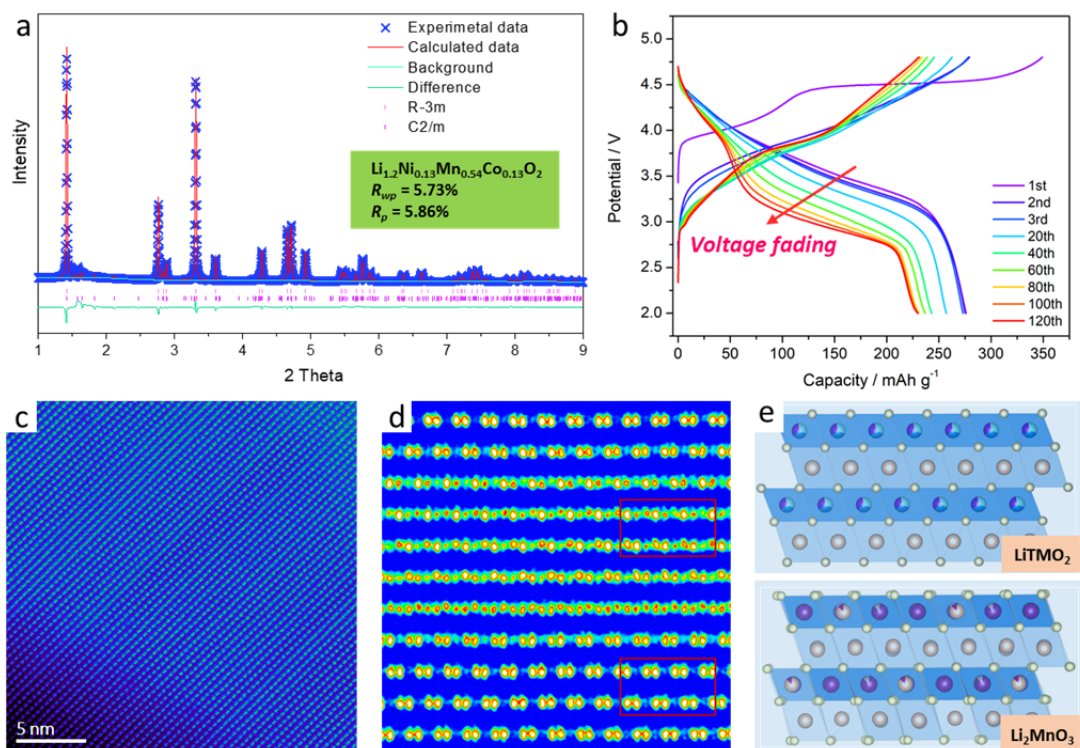
612

613

614
615

616

617

618

619

620

621

622

623

624

625

626

Figures

628

Figure 1. Electrochemical profile and initial structure of the LMR cathodes. a The XRD
pattern and Rietveld refinement results of LMR. **b** Charge / discharge curves of the LMR within
a voltage range of 2.0-4.8V at 0.1C rate current. **c** High resolution TEM image showing the
atomic arrangements of LMR. **d** Enlarged figure of the selected area of Figure 1c. **e** Schematic
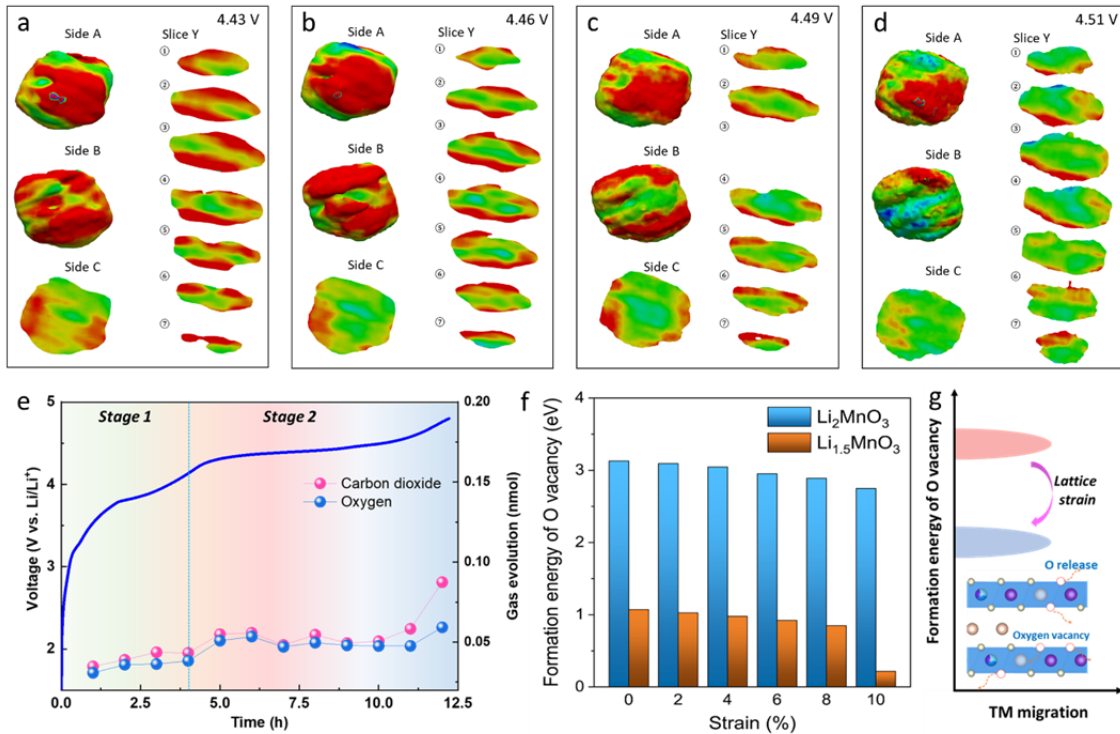structure of $LiTMO_2$ domains and Li_2MnO_3 domains.

634

635

636
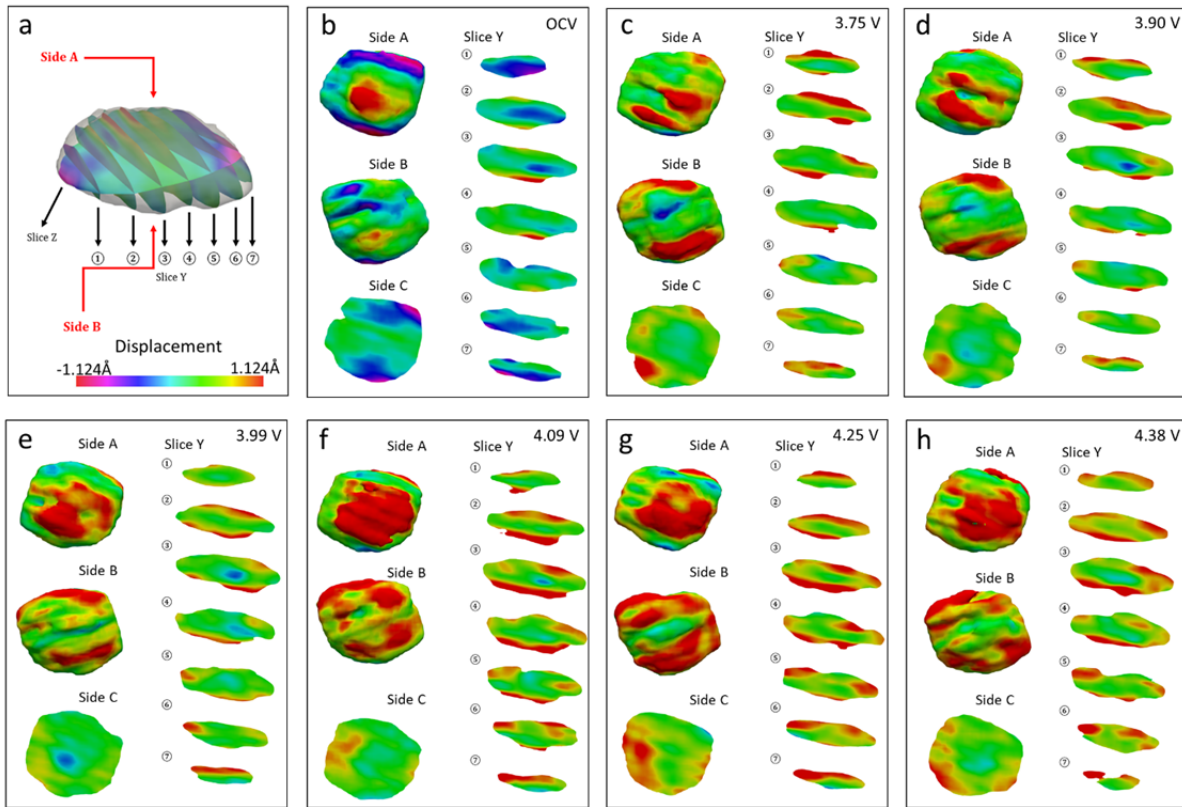
Figure 2. Strain evolution of the LMR during the charge process of stage 1. a-h *In-situ* BCDI images of the 3D LMR particle in the strain field, measured at 3.2 V (Open circuit voltage, OCV), 3.75 V, 3.90V, 3.99V, 4.09 V, 4.25V and 4.38 V, respectively. The strain evolution in each state is detailed by the spatial location of the slices along the Y axis.

641

642

Figure 3. Strain evolution of the LMR during the charge process of stage 2 and its relationship with oxygen release. a-d *In-situ* BCDI images of the 3D LMR particle in the strain field, measured at 4.43 V (OCV), 4.46 V, 4.49 V and 4.51 V, respectively. The strain evolution in each state is detailed by the spatial location of the slices along the Y axis. The color bar is same with Figure 2. **e** *In-situ* differential electrochemical mass spectroscopy measurements for LMR. **f** Formation energy of O vacancies in Li_2MnO_3 and $Li_{1.5}MnO_3$ when tensile strains are applied. **g** Schematic illustration of the influence of lattice strain on O release.
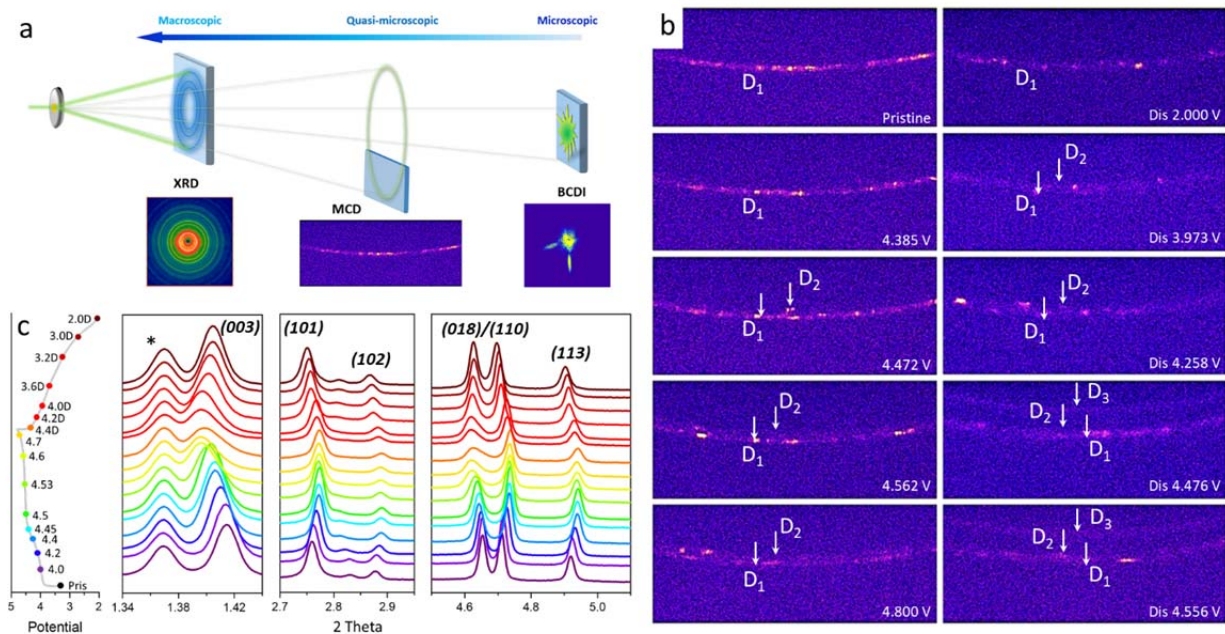
Figure 4. Multiscale X-ray diffraction techniques used to investigate the structure evolution of the LMR cathode. a Schematic of multiscale X-ray diffraction techniques used in this work. **b** *In-situ* CMCD for the (003) peak along with charge and discharge curve of the LMR cathode. Bright spots in the left figure sho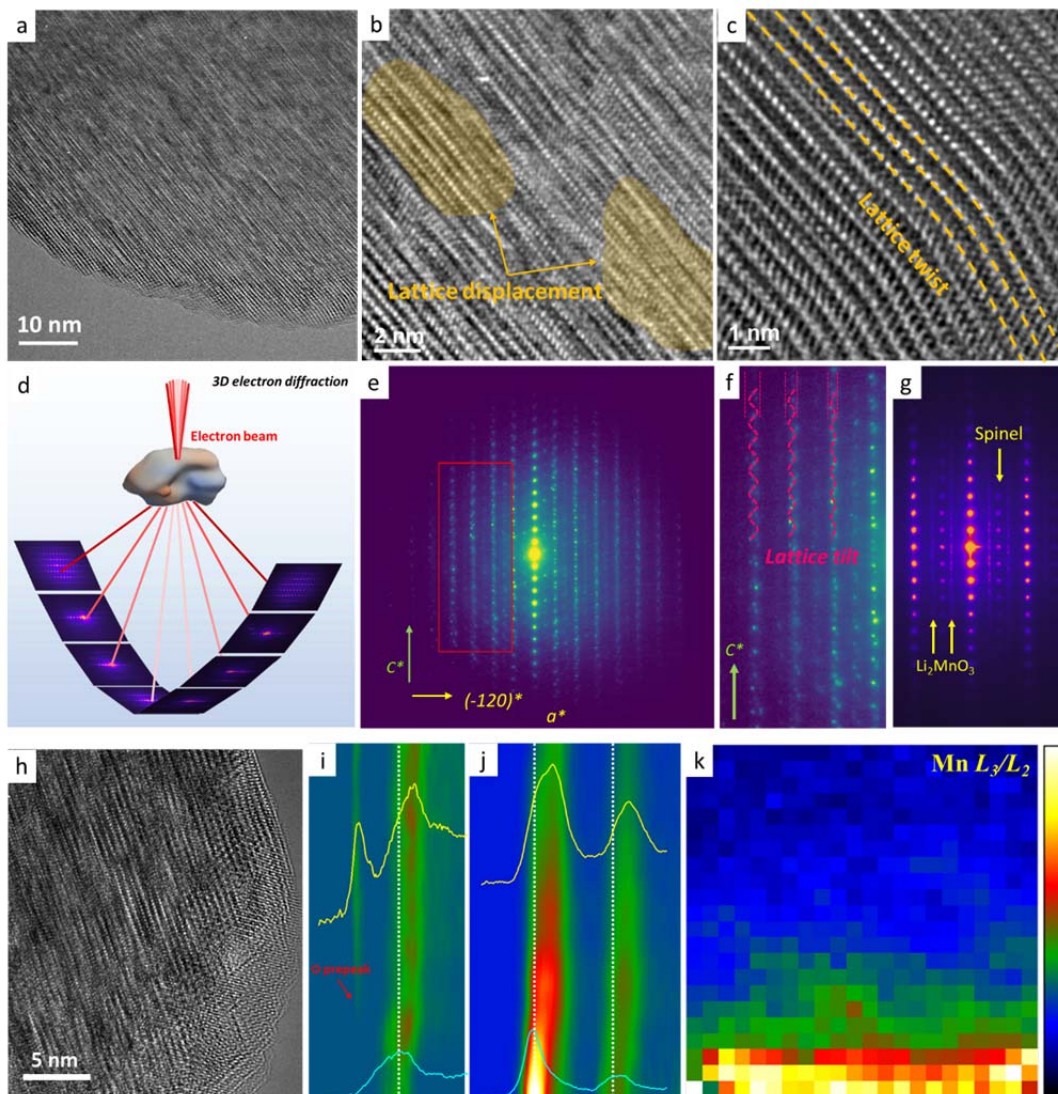w initial multi crystal diffraction corresponding to tens of particles. D_1, D_2 and D_3 correspond to three lattice distances. **c** *Ex-situ* HEXRD of the LMR cathode measured at different potentials. The peak marked by * comes from the PTFE binder.

**Figure 5. Visible observation from atomic-level TEM, 3D electron diffraction and chemical state analysis from EELS. a** Low magnification TEM image of the LMR cathode charged to 4.47 V. **b** Enlarged image of the selected area of Figure 5a. **c** High resolution TEM image of the LMR surface. **d** Schematic of the data collection process of 3D-rED. **e** Reciprocal lattice along the b^* axis of LMR. **f** Enlarged figure of the selected area of Fig. 5e. **g** SAED image of delithiated sample (4.5V) at a certain angle of rotation. **h** Low magnification TEM image of the LMR cathode charged to 4.8 V. **i** and **j** EELS line-scan of O K-edge and Mn $L_{2,3}$ edge of the LMR cathode charged to 4.8 V. **k** 2D EELS mapping of Mn K-L_3/L_2. The high value and low value colored by red and navy blue corresponds lower and higher valance state of Mn, respectively.

674

675
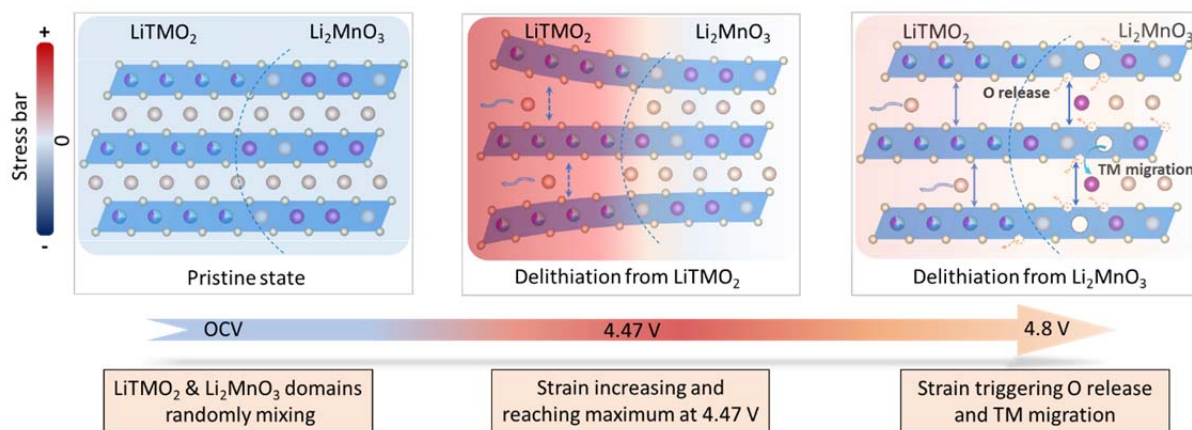
Figure 6. Schematic of the correlation of strain generation and O release as well as transition metal migration.

678

679

680

681